

Luminescence properties of ZnSe single crystals co-doped with Fe and Cr

K. Lamonova^{a,b,*}, A. Prokhorov^{c,d}, M. Schmidbauer^e, A. Kwasniewski^e, Yu Kazarinov^f,
M. Konuhova^g, A. Platonenko^g, Z. Remeš^c, K. Ridzoňová^c, M. Buryi^c

^a Max-Born-Institute for Nonlinear Optics and Short Pulse Spectroscopy, Max-Born-Straße 2A, 12489, Berlin, Germany

^b O. O. Galkin Donetsk Institute for Physics and Engineering, NAS of Ukraine, Nauky Ave. 46, 03028, Kyiv, Ukraine

^c Institute of Plasma Physics of the Czech Academy of Sciences, Za Slovankou 1782/3, 182 00, Prague, Czech Republic

^d FZU - Institute of Physics of the Czech Academy of Sciences, Na Slovance 1999/2, 18200, Prague, Czech Republic

^e Leibniz-Institut für Kristallzüchtung, Max-Born- Straße 2, D-12489, Berlin, Germany

^f NSC Kharkiv Institute of Physics and Technology, Akademichna str. 1, 61108, Kharkiv, Ukraine

^g Institute of Solid State Physics, University of Latvia, Kengaraga str. 8, Riga, LV-1063, Latvia

ARTICLE INFO

Keywords:

Co-doped ZnSe single crystals
HR-XRD
EPR
Luminescence spectra
DFT calculation
Modified crystal field theory

ABSTRACT

The luminescence properties of two co-doped ZnSe:(Cr, Fe) single crystals, grown by the Bridgman method, have been studied using photoluminescence techniques. Structural characterization by high-resolution X-ray diffraction (HR-XRD), electron paramagnetic resonance (EPR) and scanning electron microscopy (SEM) has revealed that the samples differ in terms of dopant concentration and intrinsic native defects. Analysis of the VIS and near-IR photoluminescence spectra, based on the modified crystal field theory and DFT calculations has shown that Fe and Cr exist in two charge states (+2/+3) and can be located in both tetrahedral and octahedral positions. In the blue light region, quantum dots (QDs) appear. These represent clusters of three Cr-containing octahedral complexes accompanied by Zn vacancies, anticipating the formation of spinel ZnCr₂Se₄ inclusions in the host chalcogenide ZnSe matrix.

1. Introduction

Nowadays, the wide bandgap semiconductor zinc selenide (ZnSe) and its solid solutions with transition and rare-earth metals continue to generate significant interest due to their potential applications in high-performance photoelectric [1–4] and spintronic devices [5,6]. A new intensive surge of interest has been emerged due to the advancements in technologies aimed at producing various structural forms of ZnSe, including single- and nanocrystals [7–11], film materials [12,13], nanowires [14,15], and quantum dots [16–18].

Despite a large amount of experimental and computational works, the interpretation of the photoluminescence (PL) spectra of both pure and doped ZnSe crystals is challenging. The problem lies in the complex behaviour of the dopants in the host ZnSe matrix during the solid solution formation [19–21]. The ability of Fe and Cr to embed in the interstitial space of ZnSe and readily change their valence states under the influence of external factors leads to changes in the desired dopant concentrations and the appearance of unwanted inclusions with the spinel structure [22]. Additionally, charge compensation is required,

resulting in a rearrangement of the lattice structure. In particular, a precondition for the spinel ZnCr₂Se₄ formation in the ZnSe matrix is the appearance of quantum dots (QD), clusters of three Cr-containing octahedral complexes accompanied by zinc (Zn) vacancies. It can be noticed that this phenomenon has a common character for chalcogenide matrices and has been observed, e.g., in Refs [23]. and [24]. The reason why the Cr ions form centers in octahedral cavities instead of undergoing isomorphic substitution is not completely understood.

This paper continues studying the optical properties of co-doped ZnSe: (Cr, Fe) single crystals obtained by the Bridgman method [25]. We report the PL spectrum obtained in the visual (VIS) and near-infrared (IR) wavelength regions in a wide temperature range from 290 to 4 K from the tested samples and discuss the reasons and origins of its formation. The study includes a thorough structural characterization with high-resolution X-ray diffraction (HR-XRD), electron paramagnetic resonance (EPR) and scanning electron microscopy (SEM), as well as a complex PL spectroscopic strategy and theoretical approach combining the semi-empirical Modified Crystal Field Theory (MCFT) [26] and the density functional theory (DFT) using a computational code CRYSTAL

This article is part of a special issue entitled: LUMDETR 2024 Proceedings published in Optical Materials: X.

* Corresponding author. Max-Born-Institute for Nonlinear Optics and Short Pulse Spectroscopy, Max-Born-Straße 2A, 12489, Berlin, Germany.

E-mail addresses: Karyna.Lamonova@mbi-berlin.de, k.v.lamonova@ukr.net (K. Lamonova).

<https://doi.org/10.1016/j.omx.2024.100393>

Received 13 November 2024; Received in revised form 5 December 2024; Accepted 15 December 2024

Available online 8 January 2025

2590-1478/© 2025 The Author(s). Published by Elsevier B.V. This is an open access article under the CC BY-NC-ND license (<http://creativecommons.org/licenses/by-nc-nd/4.0/>).

[27]. We believe this approach is promising as it combines the possibilities of the semi-empirical method to derive information related to the dopant properties and the ab initio method to obtain information related to the host matrix.

We have shown that the PL spectrum of the co-doped ZnSe(Cr, Fe) samples comprises two main regions: the self-activated blue spectral region caused by the near-band edge emission and the green-red spectral region related to the impurity-containing defect complexes. Cr and Fe are considered as dopants, and Mn is classified as an uncontrolled impurity. Both doped Fe and Cr can exist in two charge states (+2 and +3) and occupy both tetrahedral and octahedral positions. This leads to the formation of multiple luminescence centers in the visible (VIS), near-infrared (near-IR), and mid-infrared (mid-IR) regions. Specifically, Fe³⁺ and Cr³⁺ emit light in the green and red wavelength regions, whereas the Mn²⁺ ions are seen in the yellow-orange region.

In the blue light region, we observe the formation of QDs, which is a first step before the creation of spinel ZnCr₂Se₄ inclusions within the host chalcogenide ZnSe matrix. In addition, the formation of these quantum dots gives rise to the emergence of a Cr [1]⁺ luminescent centre, which emits light in the near-infrared region.

2. Experimental section

Samples. Co-doped ZnSe:(Cr, Fe) samples were purchased from 3photon Lithuania (ZnSe#1) and Advatech UK (ZnSe#2). The samples have been grown by the Bridgman technique; iron and chromium doping was carried out simultaneously during the process of directional solidification; Table 1. The Fe²⁺ and Cr²⁺ concentrations have been determined from optical transmission measurements. They do not point to the actual dopant concentrations but provide only the concentration of those ions incorporated into Zn sites of the metal sub-lattice.

HR-XRD and EPR characterization. High-resolution X-ray diffraction was carried out in a triple-axis setup on a 9 kW SmartLab diffractometer (Rigaku) using a four bounce Ge (220) Bartels monochromator and a two bounce Ge (220) analyzer crystal. In order to determine the lattice parameters of the samples with high absolute accuracy we have applied the modified Bond method. For more details about this technique see Ref. [28]. The samples have a sphalerite structure with the *F*4̄3*m* symmetry group and the following coordinates: Zn 4*c* – (1/4 1/4 1/4) and Se 4*a* – (0 0 0). Both samples are single crystalline. In order to check the crystal quality of the samples, a high-resolution X-ray rocking curve analysis has been carried out. The rocking curves were recorded in the vicinity of the (220) and (440) Bragg reflections at room (300 K) and close to liquid nitrogen (93 K) temperatures; Fig. 1. The ZnSe#1 sample shows a slight broadening caused the presence of a few macroscopic grains with a maximum angular spread of about 0.11°. The surface orientation is close to the (110)-plane with a small deviation of the order of 2°. The ZnSe#2 sample is 3.5 off (111) orientation but do not contains grain boundaries; see Table 1.

The temperature dependence of the lattice parameters obtained in the 100 – 300 K range shows that the ZnSe#2 lattice parameter exhibits a weak kink at 200 K and probably undergoes a slight structural rearrangement without lowering the initial symmetry; Fig. 2. We have extrapolated the HR-XRD data to zero to obtain the lattice parameters at the lowest temperatures. This is possible because the EPR data confirm

Table 1
The characteristics of ZnSe single crystals co-doped with Fe²⁺ and Cr²⁺.

Sample	Orientation	Size (mm ³)	Dopant concentration (cm ⁻³)	
			Cr ²⁺	Fe ²⁺
ZnSe#1	~2° deviation from (110); many grain boundaries	5 × 6 × 2	2 × 10 ¹⁸	2 × 10 ¹⁸
ZnSe#2	~3.5° deviation from (111); no grain boundaries	10 × 10 × 10	~10 ¹⁷	<2 × 10 ¹⁷

that both co-doped samples exhibit structural stability throughout the temperature range of 4 K < T < 450 K; see Figs. A1 and A2 in the Supplementary materials. The changes observed are not strong enough to indicate a structural transition. Thus, one can consider that the lattice parameter *a* = 5.6611 Å can be used for the further analysis of the optical spectra obtained at low temperature in both samples.

SEM analysis. The microstructural analysis of the samples was carried out using a "dual-beam" NOVA 600 system that combines a field emission gun scanning electron microscope with a gallium focused ion beam. The SEM investigations revealed that the co-doped samples are free from any contaminating phases or clusters. The EDS analysis of the sample contents showed that the element composition corresponds to the sphalerite ZnSe structure and indicated the presence of Fe and Cr, but the distribution of Fe and Cr is not uniform across the samples. In ZnSe#1, the amount of Zn is (52.28) at.% and Se is (44.33) at.% [25]. Thus, the average exhibits many native defects like V_{Se} because the number of Se positions is less than the Zn positions. ZnSe#2 has more stoichiometric composition: the average amount of Zn is (50.76) at.% and Se is (49.24) at.%.

Comparison of the XRD and SEM findings shows that the dopant concentrations are most probably not the reason for the observed difference in the lattice parameter. Indeed, sample ZnSe#1 with the lower lattice parameter exhibits a higher Fe²⁺ concentration (~2·10¹⁸ cm⁻³), while ZnSe#2 with the higher lattice parameter actually displays a lower Fe²⁺ concentration (~2·10¹⁷ cm⁻³); see Table 1. The reason for the observed difference in the lattice parameter lies in the different element compositions or the different non-stoichiometry of the samples. Since the number of Se vacancies is higher in ZnSe#1, the lattice parameter is smaller than in ZnSe#2.

EPR measurements. EPR spectroscopy studies have been carried out on a Bruker ELEXSYS E580 spectrometer at X-band (9.382780 GHz) in a wide temperature range using the ER 4122 SHQE SuperX High-Q cavity with ER 4112HV variable temperature helium-flow cryostat. The following parameters were used for the EPR measurements: modulation frequency – 100 kHz, modulation amplitude – 0.8 mT, microwave power – 0.4743 mW, conversion time – 60 ms, and spectra resolution – 4096 points.

The EPR spectra of the ZnSe#1 and ZnSe#2 samples recorded in a magnetic field $\vec{B} \parallel [110]$ at low temperatures are depicted in Fig. 3.

The EPR analysis of the ZnSe#1 sample performed in Ref. [25] revealed that Fe³⁺, Mn²⁺, Cr²⁺ and Cr³⁺ are responsible for the EPR spectrum. The analysis also indicated that Mn²⁺, Fe³⁺ and Cr²⁺ are situated in the tetrahedra, while Cr³⁺ is located in the octahedrons.

The EPR spectrum recorded from the ZnSe#2 sample shows a well-resolved hyperfine structure with nuclear spins *I* = 5/2 of ⁵⁵Mn isotope which correspond the Mn²⁺ ions located in the tetrahedral positions. The EPR spectrum can be described with a conventional spin Hamiltonian since Mn²⁺ have 3d [5] electron configuration with the full electron spin *S* = 5/2 and a 6-fold degenerated orbital singlet ⁶A as the ground state.

$$\hat{H} = g\mu_B \mathbf{B} \mathbf{S} + D \cdot \left[S_z^2 - \frac{1}{3} S(S+1) \right] + E \cdot (S_x^2 - S_y^2) + ASI. \quad (1)$$

The first term in formula (1) represents the Zeeman interaction, where **B** is the external magnetic field, μ_B is Bohr's magneton, *g* is a *g*-factor, and **S** is a full electron spin. S_x, S_y, and S_z are the fullspin projections. The second term describes the zero-field interaction with a constant *D*. The third term defines the degree of rhombicity of the system with a constant *E*. The hyperfine interaction between electrons with spin *S* and a nuclear spin *I* is described by the fourth term. In general, *A* represents an anisotropic hyperfine tensor. The last term in the spin Hamiltonian describes an HF interaction with nuclear spins *I* = 5/2 of the ⁵⁵Mn isotope.

The parameters of the spin Hamiltonian extracted using the MATLAB-based software package EasySpin 6.0.5 [29, 30] are the

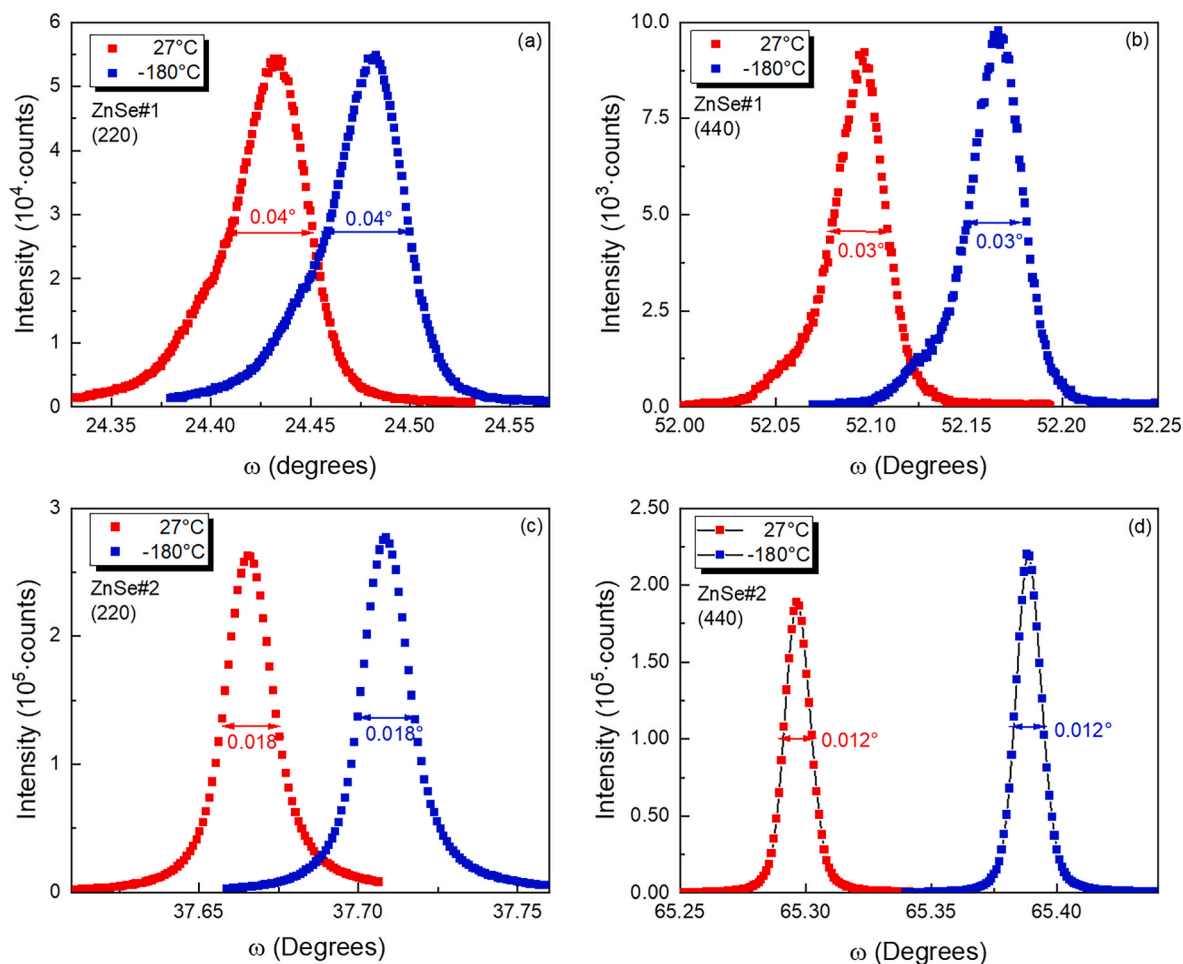


Fig. 1. Rocking curves obtained for the tested samples at the (220) and (440) Bragg reflections: (a) ZnSe#1 (220); (b) ZnSe#1 (440); (c) ZnSe#2 (220); (d) ZnSe#2 (440).

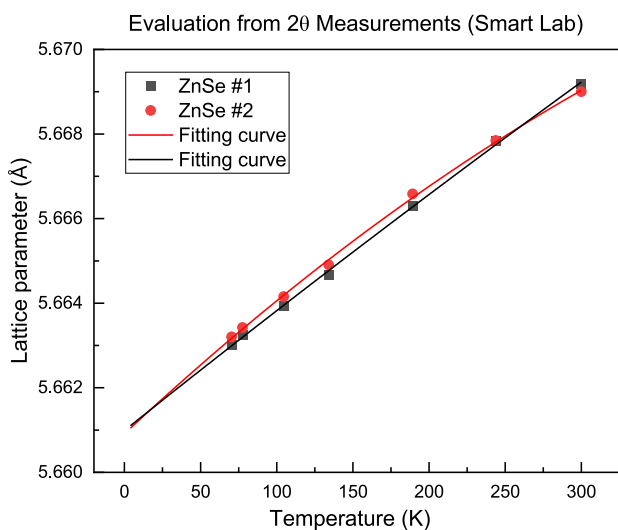


Fig. 2. Temperature dependence of the lattice parameters of the tested samples.

following: $g = 2.0091$, $A = 6.46 \pm 0.01$ mT, D and E are negligible. The final result can be explained by the fact that the Mn^{2+} ions predominantly occupy the tetrahedral positions and have the highly symmetric

ground state, which does not distort the T_d symmetry.

There are no visible EPR signals from the Cr and Fe dopants due to their low concentrations compared to Mn^{2+} in the ZnSe#2 sample.

PL measurements. Temperature-dependent photoluminescence (PL) was measured in both samples tested using a SPEX1672 double grating monochromator in the 300–800 nm spectral range with a 365 nm UV LED as the excitation source and a cooled PMT as the detector. Fig. 4a and b displays the PL spectra obtained over a wide temperature range of $4\text{ K} < T < 290\text{ K}$. Fig. 4c and d shows the decomposition of the PL spectra obtained at 4 K.

Although the samples are almost identical, the PL spectra look very different. Indeed, the samples have the same crystal symmetries. The lattice parameters are slightly different, and this difference does not affect the energy spectrum. However, the various concentrations and numbers of native defects, such as Zn vacancies, give rise to the crucial difference between these spectra.

Nevertheless, the PL spectra show the same characteristics. The PL spectra of both samples are composed of three complex bands at 400–500 nm (the blue bands), 500–600 nm (the green bands) and 600–700 nm (the red bands). The room-temperature luminescence is practically not observed; the intensity of the 400–500 nm band increases on cooling from 290 to 4 K; the 500–700 nm band forms only in the spectra below 100 K.

The blue PL band in both samples has a complicated structure and slightly shifted in the red region compared with undoped ZnSe [31, 32]; Fig. 4c and d. The pronounced near-band edge emission at 460 nm, labeled as ZnSe, appears at 100 K in both samples and is generally

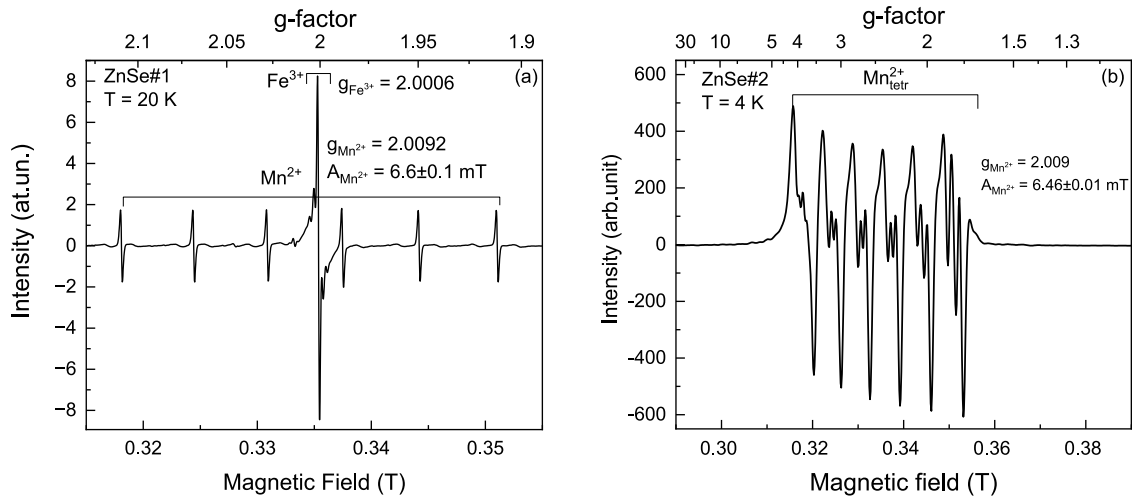


Fig. 3. EPR spectrum of the co-doped ZnSe#1 sample recorded at $T = 20$ K. (b) EPR spectrum of the co-doped ZnSe#2 sample recorded at $T = 4$ K. The operating frequency is $f = 9.382780$ GHz. The magnetic field is oriented along with the $[110]$ -axis.

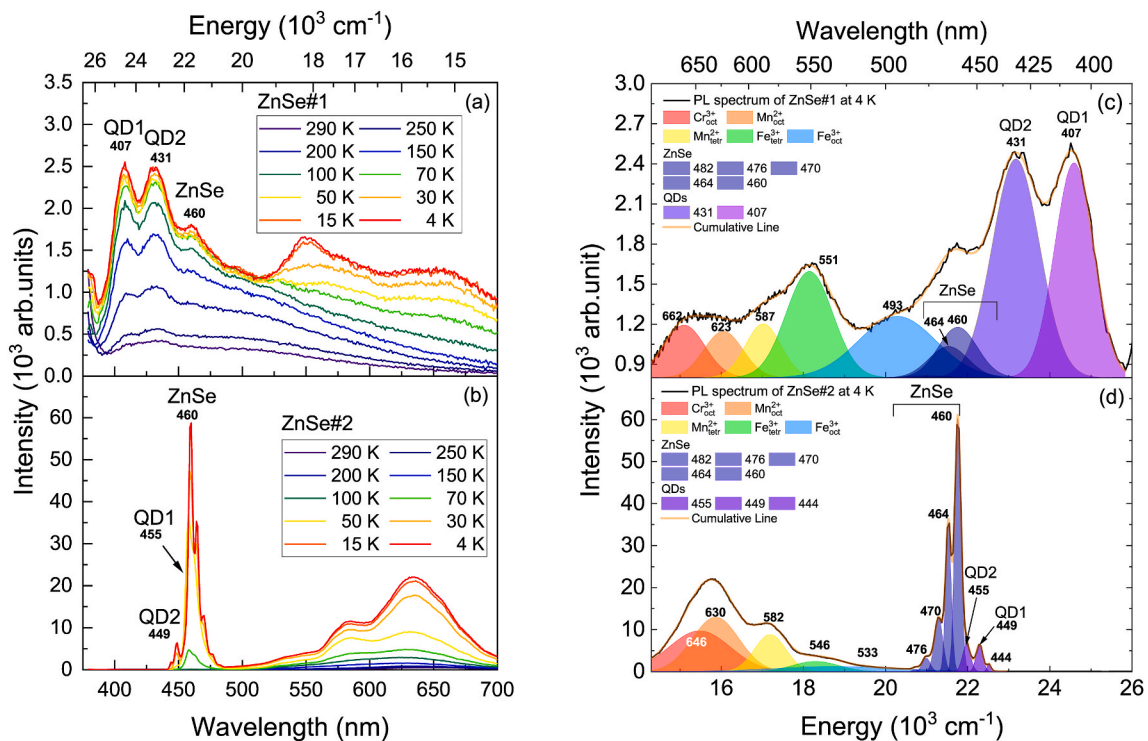


Fig. 4. PL spectra measured in the ZnSe#1 sample (a) and ZnSe#2 sample (b) under excitation in $\lambda_{ex} = 365$ nm. QD1 and QD2 denote the bands originating from the ZnSe quantum dots. ZnSe denotes the sub-bandgap luminescence of the ZnSe host. Decomposition of the low-temperature (4 K) PL spectra of the ZnSe#1 sample (c) and ZnSe#2 sample (d). See text below for descriptions. Peak maxima are given in nm.

associated with the emission of free and bound excitons [33, 34]. In particular, the three successive equidistant bands at 464, 470, and 476 nm, well-resolved on the PL spectra in Fig. 4b, are longitudinal (LO) phonon replicas of the ZnSe band. The observed averaged energy spacing of 244 cm^{-1} agreed with the LO phonon energy of 251 cm^{-1} measured by the Raman techniques for the ZnSe: (Cr, Fe) samples (is not shown here).

In addition, the blue PL band contains at least two bands of equal intensity, labelled QD1 and QD2. The positions of the QD1 and QD2 bands (407 and 431 nm in ZnSe#1; 455 and 449 nm in ZnSe#2) are in good agreement with the sub-bandgap luminescence of the ZnSe quantum dots (QD) observed, for example, in Ref. [35]. Since the bandgap of

a quantum dot is broadened as compared to a bulk crystal due to the quantum confinement effect [4, 36], the sub-bandgap luminescence maximum is blue-shifted. The size of a quantum dot influences the quantum confinement effect – the smaller the size, the larger the bandgap and the higher the emission energy, respectively [17, 18]. Therefore, the presence of two peaks (QD1 and QD2 in Fig. 4) indicates the existence of quantum dots with two different sizes. The quantum dots could be formed during the crystal growth within the crystal host. For example, the $\text{LaAl}_{11}\text{O}_{12}$ and CeAlO_3 phases appear as inclusions within crystal volumes during the crystal growth in the $\text{LaAlO}_3:\text{Ce}$ host matrix [37, 38].

We can conclude that the lower intensity of the sub-bandgap

luminescence in the case of ZnSe#1 as compared to ZnSe#2 is caused by several factors. Firstly, it is the reduced amount of the single crystal in the ZnSe#1 due to the formation of the quantum dots and, secondly, the light scattering and tunnelling at the quantum dots leading to both to the re-absorption and non-radiative transitions. Note that QDs are difficult to detect by HR-XRD when their concentration in the host material is low [39].

Finally, the green and red bands are related to the emission of impurity-containing complexes [40] and references therein. To define what kind of impurities contribute to the PL spectra in the visual range, we have decomposed the low temperature PL spectra. We found that Fe^{3+} , Cr^{3+} and Mn^{2+} appear in the spectra in different environments. Cr^{3+} is only found in an octahedral selenide cage, Mn^{2+} and Fe^{3+} can be found in both tetrahedral and octahedral positions.

IR-PL measurements. To get more information about the samples, infrared (IR) photoluminescence has been measured as well. The IR PL spectra were measured at room temperature in the range of 550–1100 nm using a Horiba H20IR grating monochromator. A 532 nm laser was used as an excitation source and a Si photodiode as a detector. To achieve a better spectral resolution, some of the IR PL spectra were also measured using a Nicolet iS50 FTIR spectrometer (Thermo Fisher Scientific) equipped with an FT Raman module with the 1064 nm laser and InGaAs photodiode detector. The IR PL spectra of both samples are shown in Fig. 5.

Both spectra consist of a broad band in the visual 500–850 nm region and a pronounced band in the near IR region of 850–1100 nm. As in Fig. 4, the spectral bands have different intensities related to the different dopant concentrations. The decomposition of the IR-PL spectra

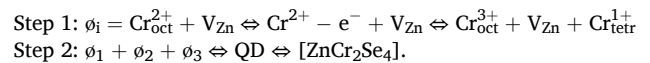
indicates the presence of impurity-containing complexes in the samples. The broad near-IR band suggests the appearance of Cr^{1+} ions in the tetrahedral positions caused by the formation of the quantum dots and the further clustering process.

3. Results and discussion

Analysis of the co-doped ZnSe (Cr, Fe) structure. Although a ZnSe compound exhibits a very simple cubic crystal structure, a number of problems arise with transition metal doping [23, 24, 25, 41, 42]. First of all, it is a problem related to the formation of the Frenkel defects. In particular, under Cr and Fe doping, it is expected that Cr and Fe will have charge state +2, substitute Zn^{2+} and occupy tetrahedral positions. However, the dopant ions can embed in the interstitial space and form the Frenkel defects written in accordance with the Kröger–Vink notation like $\phi = (\text{Cr/Fe})_i^{2+} + V_{\text{Zn}}''$ (where i denotes interstitial space and V_{Zn}'' is a two-charged Zn vacancy) as shown in Fig. 6a. The same applies to Mn ions, which are present in the tested samples as uncontrolled impurities. The other problem is linked to the different solubilities of foreign atoms in chalcogenide matrixes. If the doped ions are well dissolved in a host matrix, a homogeneous solid solution is formed [41–44]. If impurity ions are weakly dissolved in a host matrix, the nanoclusters with the spinel structure can be formed around them [22, 23, 24]; see Fig. 6b. The last problem is that the Cr and Fe ions readily change their charge state by adapting to the crystalline environment or reacting to temperature. For example, the charge transfer $\text{Fe}^{2+} \leftrightarrow \text{Fe}^{3+}$ occurs as a result of a self-ionization process [42, 45] and Cr^{3+} appears due to a clustering process. Thus, Cr and Fe embedded in the host ZnSe matrix can occupy both tetrahedral and octahedral positions and change their charge states, giving rise to four different paramagnetic subsystems: $\text{Fe}^{2+}/\text{Fe}^{3+}$ and $\text{Cr}^{2+}/\text{Cr}^{3+}$.

The incorporation of Fe into the interstitial space does not lead to the formation of any other crystalline phases, whereas the incorporation of Cr leads to the formation of spinel phase inclusions. In general, the clustering occurs in two steps depending on the Cr concentration. The quantum dots are formed at low Cr concentrations. As the Cr concentration increases, spinel clusters are formed. In the first step, two or three Cr^{2+} ions cluster together in the interstitial space forming Frenkel defects; see Fig. 6b. Being in the octahedral position, they change their charge state from +2 to +3 and release extra electrons into the ZnSe crystal. These extra electrons are captured by the nearest Cr^{2+} and as a result, Cr^{1+} ions settle in the nearest tetrahedrons. The Cr^{3+} ions begin to interact with each other as quantum dots and can be seen in the blue band in Fig. 4.

In the second step, as the Cr concentration increases, the nanoclusters with the spinel structure are formed based on these quantum dots. Thus, the QDs are the prerequisite for the formation of a new ZnCr_2Se_4 spinel phase. The process can be written like:



DFT analysis. First-principles calculations have been performed using the CRYSTAL23 code [12] within the Linear Combination of Atomic Orbitals (LCAO) approximation and using the hybrid PBE0 exchange-correlation functional [46, 47]. The POV-TZVP-rev2 basis sets [48] were applied for Zn and dopant ions (Mn, Fe, Cr); for the Se ions, we use the pseudopotential effective-core basis set ECP28MDF of Dolg et al. [49] together with the corresponding (4s4p4d)/[3s3p2d] valence basis [50]. A homogeneous neutralising charge background was used to calculate charged defects.

We have calculated the band structure and total density of states for the cubic ZnSe sphalerite and ZnCr_2Se_4 spinel structures; see Fig. 7. The lattice parameters of 5.6611 Å and 10.54 Å are applied for ZnSe and ZnCr_2Se_4 respectively. The band gap for ZnSe was found to be 2.91 eV

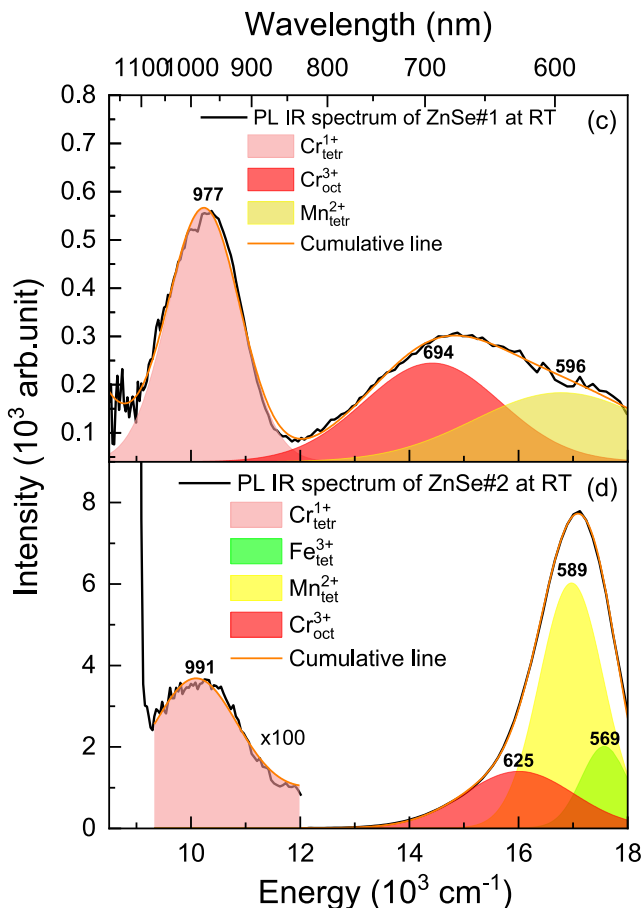


Fig. 5. IR-PL spectra of ZnSe#1 and ZnSe#2 samples obtained at room temperature. The excitation wavelength is 532 nm.

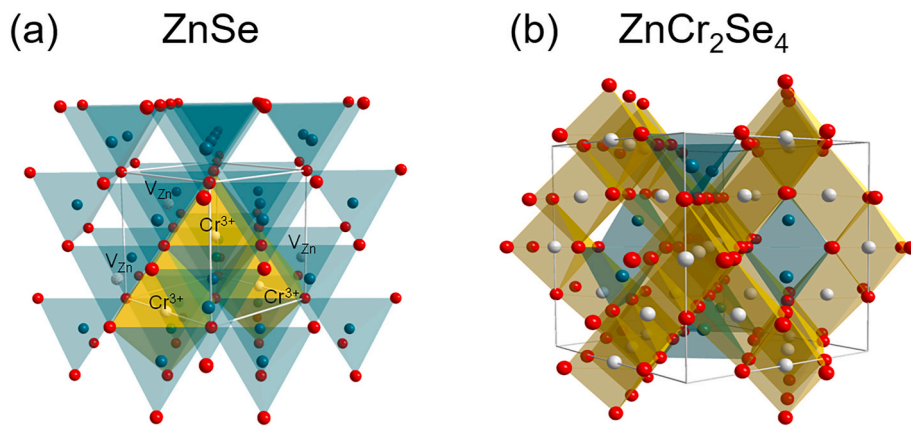


Fig. 6. Elementary cells of a ZnSe sphalerite (a) with three ions of Cr³⁺ ions embedded in the interstitial space and a ZnCr₂Se₄ spinel (b) structures.

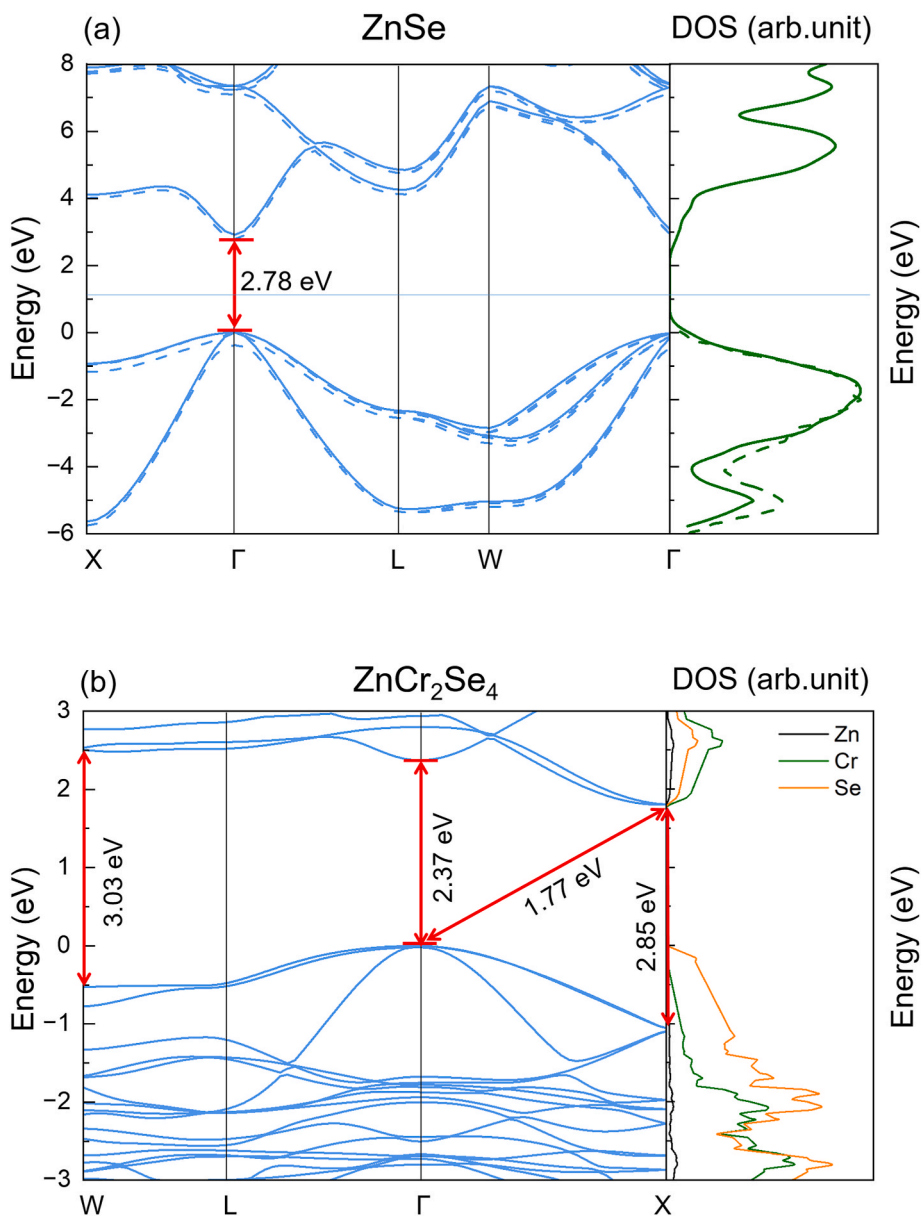


Fig. 7. The band structure and total density of states calculated for an undoped cubic ZnSe (a) sphalerite and ZnCr₂Se₄ spinel structures (b). The dashed line is the ZnSe band structure determined by spin-current density functional theory. In the density of states (DOS) plot for ZnSe, the calculated and smothened DOS are shown in solid, and the dashed line is experimentally measured XPS data [56].

without considering the spin-orbit interaction. Inclusion of the spin-orbit interaction into consideration using a spin current DFT formulation [50–54] results in a reduction of the band gap to 2.78 eV, which is due to the lowering of the conduction band bottom. The spin-orbit splitting energy of the valence band at the Γ -point of 0.38 eV, which is in good agreement with the experimentally measured value of 0.40 eV [55]. The splitting also affects the highest valence band within the entire first Brillouin zone.

The direct band gap of the ZnCr_2Se_4 spinel structure in the Γ -point is 2.37 eV. Additionally, there are possibilities for indirect transitions through Γ -to X-points due to the less band gap of 1.77 eV.

The CRYSTAL23 code was used to determine the energies of defect formation in the tested samples. A periodic $2 \times 2 \times 2$ supercell consisting of 64 atoms was used to simulate isolated defects in the crystal lattice. The defect formation energy E_f is calculated according to the following equation [57]:

$$E_f = E_D - E_p - \mu_{\text{Me}} + \mu_{\text{Zn}}.$$

In our calculations, E_D represents the total energy of the defect supercell, and E_p indicates the total energy of the pristine supercell. The chemical potentials for the cations are denoted as μ_{Zn} and μ_{Me} . For the chemical potential of selenium μ_{Se} , we use the energy of a single atom in the selenium crystal. Additionally, the chemical potential for a dopant ion μ_{Me} is derived from the total energy of the corresponding MeSe selenide in its ferromagnetic phase.

The formation energies of Mn (~ 0.01 eV) and Fe (~ 0.02 eV) substitution defects ($\text{Me}^{2+} \rightarrow \text{Zn}^{2+}$) are close to zero, indicating that these impurities are freely soluble in a ZnSe matrix. In contrast, the substitution of Zn by Cr is more challenging and requires 0.59 eV. The calculated energies of the defect complexes $\text{Me}_{\text{tet}}^{2+} + V_{\text{Zn}}$ show that the binding of Cr^{2+} substitution defects to a nearest Zn vacancy is energetically favourable (-17.8 eV), whereas for Fe and Mn defects this process is endothermic and takes 8.8 and 68.8 eV, correspondingly. Additionally, the formation of a Frenkel defect like $\phi = \text{Cr}_{\text{oct}}^{2+} + V_{\text{Zn}}''$ requires 3.61 eV. As a result, Cr tends to change its charge state to +3 when in an octahedral position [58]. Multiple edge-shared $[\text{Cr}^{3+}\text{Se}_6]$ octahedrons can cluster together, serving as a seed for the formation of the spinel ZnCr_2Se_4 inclusions [22].

We also analyzed the positions of the electronic states associated with substitutional defects concerning the band gap. Fig. 8 illustrates that Mn and Fe substitutional defects do not generate electronic states within the band gap. Instead, their d-states are located within the valence band. The unoccupied d-states of Mn and Fe are found close to the bottom of the conduction band. It can be expected that when an

electron is trapped at these levels, it will move into the band gap following further radiative relaxation. The electronic states of Cr ions and Zn vacancies can be found within the band gap. For Cr^{2+} ions located in tetrahedral positions, the occupied states are positioned just above the valence band, while the unoccupied states are near the bottom of the conduction band. In the case of Cr^{1+} ions, which are also in tetrahedral positions, their energy levels reside in the middle of the band gap. Conversely, when Cr^{3+} ions occupy octahedral positions, we only observe unoccupied states within the band gap, with the occupied states located deep within the valence band. Studying the defect complexes ($\text{Me} + V_{\text{Zn}}$), we observed that vacancy defect has almost no effect on the d-states of impurity ions.

MCFT: basic statements and parameters of the problem. We applied the modified crystal field theory to confirm the presence of $\text{Cr}^{2+}/^{3+}$, $\text{Fe}^{2+}/^{3+}$, and Mn^{2+} in the PL and IR-PL spectra shown in Figs. 3 and 4. MCFT is a semi-empirical numerical method for calculating the electron energy levels of paramagnetic ions embedded in a coordination complex of arbitrary symmetry. We have detailed the main statements of the MCFT in the monograph [26]. Here, we briefly mention the following points.

Similar to the conventional crystal field theory, we consider a paramagnetic ion in a crystal potential, which is created by the electrons and nuclear charges surrounding a paramagnetic ion. The point charge approximation is valid. All calculations are carried out within the single-configuration approximation. The model utilizes the many-determinant wave functions constructed from hydrogen-like functions to describe the electron states of an unfilled shell of a paramagnetic ion. The Born-Oppenheimer approximation is inherently assumed, i.e., the eigenfunctions used to construct a solution are parametrically dependent on the positions and charges of ligands. All the relativistic interactions and the interaction with an external magnetic field can be taken into account within the MCFT.

The parameters of the problem are an *effective nuclear charge* of a paramagnetic ion and a constant for accounting for the relativistic interactions. The effective nuclear charge is an averaged parameter characterizing the Coulomb's field of the core, which is simultaneously modified in the presence of a cloud of ligand electrons. It gives the opportunity to implicitly account for the influence of ligand electrons, or, in other words, the covalence degree of a «paramagnetic ion–ligand» bond. It significantly enhances the predictive capabilities of the modified crystal field theory.

Thanks to the simple parameterization MCFT makes it possible to investigate coordination complexes with arbitrary symmetry and a set of ligands, to study various types of distortions of the coordination complex by modelling their effect on the electron states of the system, as well as to investigate the evolution of the electron structure under the influence of external parameters such as pressure, temperature, and magnetic field. Applying MCFT, one can get information about spin and orbital states of a paramagnetic ion, calculate g-factors for analyzing EPR spectra [23, 41, 42] and also the intensity of magneto-dipole transitions for analyzing the spectra of optical absorption and luminescence [25, 59].

Finally, the calculated spectrum depends on parameters describing the paramagnetic ion and the coordination complex. In other words, we need to know the coordinates and charges of the ligands, the parameter characterizing the relativistic interactions, and the value of an effective nuclear charge of a paramagnetic ion in a host matrix Z_{eff} .

Thus, for the MCFT calculations, we use the ligand coordinates for both samples with $a = 5.6611$ Å. The ligand charges are assumed to be -2 , given the oxidation state of the selenide. The one-electron constants of the spin-orbit interaction for the dopants Cr^{3+} , Cr^{1+} , Fe^{3+} , and the uncontrolled impurity Mn^{2+} depend on the Z_{eff} as follows $\xi_{3d}^{\text{calc}} \sim Z^{2-\beta} Z_{\text{eff}}^2$ [60], where the parameter Z is a nuclear charge and β are equal to $\beta_{\text{Cr}^{3+}} = 0.13$, $\beta_{\text{Cr}^{1+}} = \beta_{\text{Fe}^{3+}} = \beta_{\text{Mn}^{2+}} = 0.06$. The calculated spin-orbital constants for the free ions are in a good agreement with the

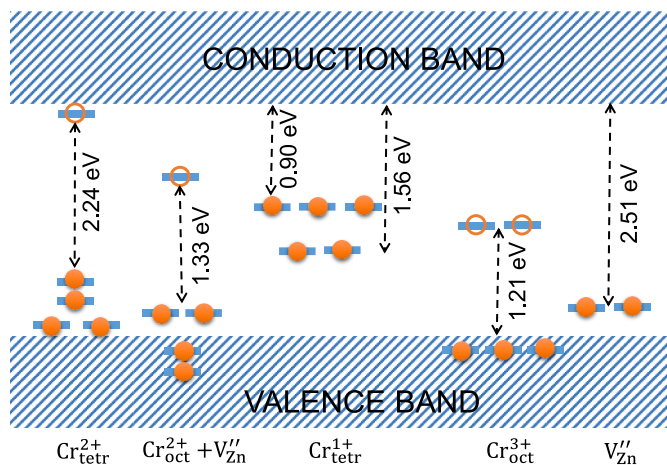


Fig. 8. Electronic defect states generated by chromium and zinc vacancy defects in the ZnSe matrix. Only states within the band gap are shown. Filled circles represent filled states, while empty circles represent unfilled states.

experimental values $\xi_{Cr^{3+}} = 288 \text{ cm}^{-1}$, $\xi_{Cr^{1+}} = 189$, $\xi_{Fe^{3+}} = 485 \text{ cm}^{-1}$ and $\xi_{Mn^{2+}} = 342 \text{ cm}^{-1}$ [61, 62], correspondingly. The other characteristics of the tested ions are given in Table 2. Note that the spin-orbital constants are reduced in the crystal field due to the ligand charges, which provide additional shielding of the Z_{eff} of a paramagnetic ion.

MCFT analysis. Table 2 shows characteristics the octahedral and tetrahedral coordination complexes in the co-doped ZnSe samples and also Fe^{3+} , Cr^{3+} and Mn^{2+} ions. According to Table 2, the Cr^{3+} , Fe^{3+} or Mn^{2+} ions embedded in the interstitial space of ZnSe become 6-fold coordinated. The large octahedral volume weakens the influence of the octahedral crystal field on these ions. However, they can move from the symmetry center of the coordination complex towards the associated vacancy in the next coordination sphere; see Fig. 6a. Conversely, when the Cr^{1+} , Fe^{3+} or Mn^{2+} ions replace Zn^{2+} in the tetrahedra, they feel a sufficiently strong crystal field from the surrounding selenide cage to prevent any displacements from the symmetry center.

The presence of Cr^{1+} , Fe^{3+} , and Mn^{2+} in the ZnSe matrix does not cause low-symmetry distortions of the selenide cage, as these ions have a spherically symmetric 6S ground state. Conversely, Cr^{3+} has a small ionic radius and a strongly anisotropic 4F ground state—the first results in displacements of Cr^{3+} ions from the octahedral center, and the second causes low-symmetry distortions of the selenide octahedron. Additionally, the presence of V_{Zn} in the nearby coordination sphere violates the electrostatic equilibrium and results in its deformation.

We have calculated the energy diagrams of the Fe^{3+} , Cr^{3+} , Mn^{2+} and Cr^{1+} ions located in the selenide tetrahedra and octahedra, depending on the effective nuclear charge Z_{eff} . The diagrams can be found in the Supplementary material in Figures B1-B6, showing the energy levels up to $6 \cdot 10^4 \text{ cm}^{-1}$. For Cr^{3+} in the octahedrons (Figure B5), the energy range is restricted to $4 \cdot 10^4 \text{ cm}^{-1}$. Experimental excitation wavelengths $\lambda_{ex} = 365 \text{ nm}$ (or 27397 cm^{-1}) and $\lambda_{ex} = 532 \text{ nm}$ (or 18797 cm^{-1}), as well as the peak values of the PL and IR-PL transitions in Fig. 4a and 5, are depicted by red dash lines and red solid arrows. The obtained results are summarized in Table 3.

The diagrams in Figures B1-B6 and Table 3 indicate that the luminescence bands observed in Figs. 4 and 5 can be attributed to the dopant ions Fe and Cr, as well as the impurity ions of Mn. The Fe ions exist in a charge state of +3 and occupy both tetrahedral and octahedral positions. The Cr ions can have charge states of +3 and +1, with +3 occupying the octahedral positions and +1 occupying the tetrahedral positions. The Mn ions are incorporated in the host ZnSe matrix as +2 ions and predominantly occupy the tetrahedral positions, although a fraction can also be found in the octahedral positions.

According to Fig. 4b and Table 3, the determined band positions for the Mn and Cr ions' bands as well as Fe^{3+} in the tetrahedral positions have very close energies. Given this, we can use a single value for Z_{eff} for both samples, except the Fe^{3+} ions are in octahedral positions. The energy difference between the bands is approximately 1600 cm^{-1} , which complicates the accurate determination of Z_{eff} due to the low intensity

Table 2
Characteristics of manganese, iron and chromium ions.

Ionic radii (R_{ion}) based on Shannon's data [63] and [64]					
Octahedral [MSe_6] complex, $M = Cr^{3+}, Cr^{1+}, Fe^{3+}$ and Mn^{2+}			Tetrahedral [MSe_4] complex, $M = Cr^{3+}, Cr^{1+}, Fe^{3+}$ and Mn^{2+}		
Cr^{3+}	Fe^{3+}	Mn^{2+}	Cr^{1+}	Fe^{3+}	Mn^{2+}
$S = 3/2$	$S = 5/2$	$S = 5/2$	$S = 5/2$	$S = 5/2$	$S = 5/2$
0.618 Å	0.645 Å	0.83 Å	>0.66 Å	0.49 Å	0.66 Å
The ground term, ^{2S+1}L					
4F	6S	6S	6S	6S	6S
Difference between R_{ion} of an embedding TM ion and the bond lengths					
$R(\theta-Se) = 2.8348 \text{ Å}$			$R(Zn-Se) = 2.4550 \text{ Å}$		
$R_{ion}(Se^{2-}) = 1.98 \text{ Å}$			$R_{ion}(Zn^{2+}) = 0.60 \text{ Å}; R_{ion}(Se^{2-}) = 1.98 \text{ Å}$		
-0.2363 Å	-0.2098 Å	-0.0248 Å	>0.185 Å	0.015 Å	0.185 Å

* $R(Zn-Se)$ is a bond length; $R(\theta-Se)$ is a distance from the center of an octahedron (θ) and Se; R_{ion} is an ionic radius.

Table 3
Characteristics of the found PL centers.

PL centers	Fe^{3+}_{tet}	Fe^{3+}_{oct}	Mn^{2+}_{tet}	Mn^{2+}_{oct}	Cr^{3+}_{oct}	Cr^{1+}_{tet}
ZnSe#1						
λ , nm	551	493	587	623	662	977
E , cm^{-1}	18149	20284	17036	16051	15106	10235
ZnSe#2						
λ , nm	546	533	582	630	646	991
E , cm^{-1}	18315	18716	17082	15873	15480	10091
Z_{eff}	5.43	<5.66>	5.21	5.17	5.44	4.45

and broad width of the Fe^{3+} band in the ZnSe#2 sample, as shown in Fig. 4b.

The presence of Fe^{3+} in tetrahedral and octahedral positions of the ZnSe matrix is caused by the temperature-induced charge transfer and confirmed by the EPR analysis made in Ref [42] and also in the works of other authors [65, 66].

A signal from Cr^{3+} as a part of spinel inclusions has been recorded in the EPR spectrum of the Cr-doped HgSe matrix [23] and also in ZnSe#1 (i.e., co-doped ZnSe:(Cr, Fe) single crystal) in our earlier work [25]. The other authors confirm the existence of the +3 charge state of Cr in various chalcogenide matrices; see e.g. [58, 67]. The EPR signals of Cr^{1+} in a ZnSe matrix have been indicated using time-dependent photo-EPR method as a result of Cr charge transfer processes [68].

In addition, we have recorded the presence of Mn^{2+} in two crystallographic positions. In particular, Mn^{2+} in the tetrahedral positions gives the band at 587 and 582 nm in ZnSe#1 and ZnSe#2 samples, respectively. These emission band positions are similar to those for Mn^{2+} in bulk [69, 70] and nanocrystalline [71] ZnSe samples. Mn^{2+} in the octahedral positions emits in the orange region at 632 and 630 nm. The presence of Mn^{2+} in the octahedral positions has been observed in the EPR spectrum of Fe doped ZnSe [42]. Also in Ref. [72], EPR and optical absorption studies showed that the site symmetry of Mn^{2+} in Mn^{2+} doped ZnSe nanoparticles is predominantly octahedral.

To provide a comprehensive understanding, we calculated the energy levels of all the ions involved at the specified Z_{eff} and presented the results in Fig. 9. The energy levels for the ions are confined to a range of $3.5 \times 10^4 \text{ cm}^{-1}$ to enhance clarity.

The calculations show that the observed luminescence transitions are spin-forbidden. In particular, there is a $^4T_2(G) \rightarrow ^6A_1(S)$ transition in Fe^{3+} , Mn^{2+} and Cr^{1+} and a $^2A_1(G) \rightarrow ^4A_2(F)$ transition in Cr^{3+} . It is seen in Fig. 9 that the octahedral [$Cr^{3+}Se_6$] complex, as calculated using the XRD data, does not align well with the experimental PL band. This discrepancy can be attributed to three main reasons: (i) Cr^{3+} has a small ionic radius (0.615 Å) compared to a large selenide cage; (ii) the ground orbital state of Cr^{3+} is a highly anisotropic 4F term; (iii) a zinc vacancy in the nearby coordination sphere.

These factors significantly distort the [$Cr^{3+}Se$] [6] coordination complex, and the Cr^{3+} can move away from the center of the octahedron.

4. Conclusions

Our investigations of the co-doped ZnSe:(Cr, Fe) samples have revealed that the incorporation of Cr and Fe into the host ZnSe matrix is a complex process leading to the formation of several luminescence centers. Firstly, there is a well-known process where Cr^{2+} and Fe^{2+} replace Zn^{2+} in tetrahedral complexes and emit in the mid-IR region. Fe^{2+} can easily change its charge state due to the temperature-induced charge transfer $Fe^{2+} \leftrightarrow Fe^{3+}$, and Fe^{3+} in the tetrahedra emits green light at 551–556 nm. We did not detect any evidence of Cr^{3+} in the tetrahedra.

Another process involves the formation of Frenkel defects such as $\theta = (Cr/Fe)_{tet}^{2+} + V_{Zn}^{2-}$, when Cr^{2+} and Fe^{2+} occupy the interstitial space.

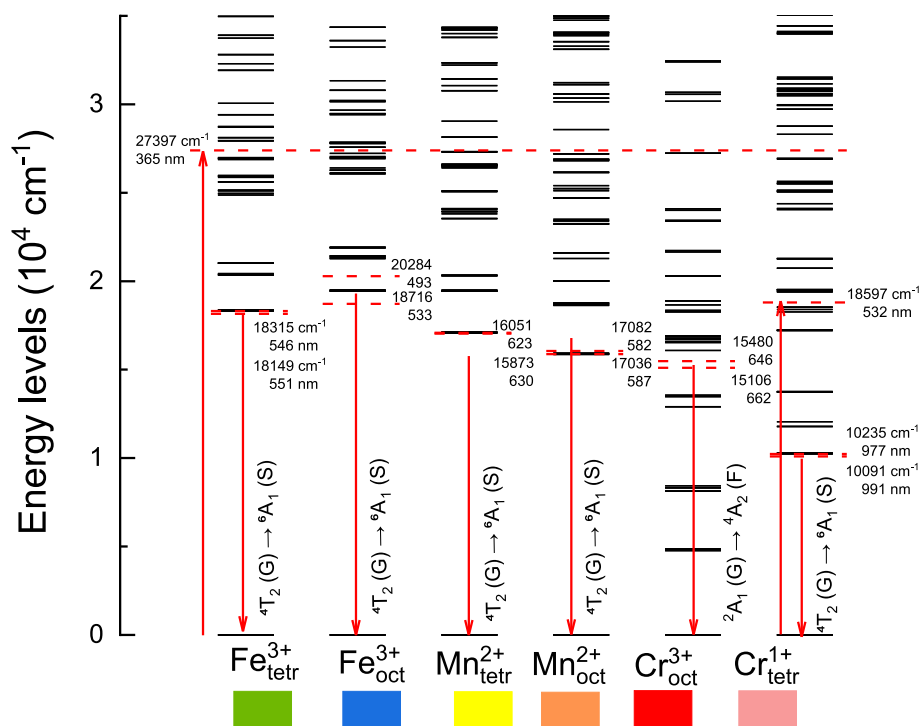


Fig. 9. Scheme of the energy levels of the optical transitions in the co-doped ZnSe: (Cr, Fe) single crystals. The energy levels of Fe^{3+} , Mn^{2+} , Cr^{3+} , and Cr^{1+} ions located in tetrahedral and octahedral complexes. The MCFT calculations have been carried out for different values of Z_{eff} ; see Table 3 and the explanation in the text.

Cr^{2+} changes its charge state up to +3. The extra electron then transfers to the nearest Cr^{2+} in a tetrahedron forming a Cr^{1+} luminescent center. As a result, Cr^{3+} in the octahedrons emits in the red region at 646–662 nm, and Cr^{1+} in a tetrahedron can be detected in the near-IR region at 977–991 nm. Fe^{3+} in the octahedrons is seen in the green-blue region at 493–533 nm.

We also found two emission bands from Mn ions presented in the samples as an uncontrolled impurity. Mn^{2+} located in the tetrahedrons emits in the yellow region at 582–587 nm, and Mn^{2+} located in the octahedrons is seen in the orange region at 623–630 nm.

The PL bands observed in the blue region at 480–460 nm have been identified as emissions from free and bound excitons. We have linked the prominent bands at 401 and 407 nm in ZnSe#1 and 445 and 449 nm in ZnSe#2 to the formation of the QDs, which represent the first step in the development of the spinel ZnCr_2Se_4 structure in the host ZnSe matrix.

CRedit authorship contribution statement

K. Lamonova: Writing – original draft, Supervision, Methodology, Conceptualization. **A. Prokhorov:** Investigation. **M. Schmidbauer:** Investigation, Formal analysis. **A. Kwasniewski:** Investigation. **Yu Kazarinov:** Investigation, Formal analysis. **M. Konuhova:** Data curation. **A. Platonenko:** Software, Formal analysis. **Z. Remes:** Investigation. **K. Ridzoňová:** Investigation. **M. Buryi:** Writing – review & editing, Writing – original draft, Methodology, Conceptualization.

Author agreements

All authors of the manuscript have checked the manuscript and have agreed to the submission.

Declaration of competing interest

The authors declare that they have no known competing financial interests or personal relationships that could have appeared to influence the work reported in this paper.

Acknowledgements

Dr. Sci. Karyna Lamonova would like to thank the Deutsche Forschungsgemeinschaft (German Research Foundation) for funding this work (project No. 517713174). Financial support from the Czech Science Foundation (project No 24–10607J) is gratefully acknowledged. We are thankful to Mrs. Sabine Bergmann (Leibniz-Institut für Kristallzüchtung Berlin, Germany) for her technical assistance. The authors thank Dr. Sci. Serhii Orel for the support of the MCFT software. We thank the European Regional Development Fund (ERDF, project No. 1.8/15). Finally, M. Konuhova and Aleksandr Platonenko acknowledge LZP grant 2023/1-0453.

Appendix A. Supplementary data

Supplementary data to this article can be found online at <https://doi.org/10.1016/j.omx.2024.100393>.

Data availability

Data will be made available on request.

References

- [1] R.N. Bhargava, Materials growth and its impact on devices from wide band gap II–VI compounds, *J. Cryst. Growth* 86 (1988) 873–879, [https://doi.org/10.1016/0022-0248\(90\)90817-5](https://doi.org/10.1016/0022-0248(90)90817-5).
- [2] R.A. Reynolds, J. Vat, *Sci. Technol. A* 7 (1989) 269–270, <https://doi.org/10.1116/1.576109>, and references therein.
- [3] L.D. DeLoach, R.H. Page, G.D. Wilke, S.A. Payne, W.F. Krupke, Transition metal-doped zinc chalcogenides: spectroscopy and laser demonstration of a new class of gain media, in: *IEEE J. Quant. Electron.*, vol. 32, 1996, pp. 885–895, <https://doi.org/10.1109/3.502365>.
- [4] P. Facci, Semiconductor nanocrystals from Langmuir-Blodgett films: synthesis, characterization, and applications, in: Hari Singh Nalwa (Ed.), *Handbook of Surfaces and Interfaces of Materials*, Academic Press, 2001, pp. 281–310, <https://doi.org/10.1016/B978-012513910-6/50040-2>.
- [5] I. Malajovich, J. Berry, N. Samarth, et al., Persistent sourcing of coherent spins for multifunctional semiconductor spintronics, *Nature* 411 (2001) 770–772, <https://doi.org/10.1038/35081014>.

- [6] V.N. Jafarova, N.T. Mamedov, M.A. Musaev, High Curie temperature and half-metallic ferromagnetism in ZnSe: Co, Ni with wurtzite structure: first-principles study, *Phys. Status Solidi* 260 (2023) 2200360, <https://doi.org/10.1002/psb.202200360>.
- [7] W. Nan, Da Yang, B. Zhou, Qi Fu, H. Yu, Z. Hu, Ji Wang, Yi Wu, Growth and characterization of Fe²⁺:ZnSe single crystals for tunable mid-infrared lasers, *J. Cryst. Growth* 614 (2023) 127230, <https://doi.org/10.1016/j.jcrysgro.2023.127230>.
- [8] A. Akyzbekova, et al., Annealing effect on structural, optical and electrophysical properties of ZnSe nanocrystals synthesized into SiO₂/Si ion track template, *Materials* 17 (2024) 4149, <https://doi.org/10.3390/ma17164149>.
- [9] Sh Chen, R. Yu, L. Song, R. Zhang, X. Cao, B. Wang, P. Zhang, Effect of low temperature vulcanization time on the structure and optical properties of ZnS thin films, *Appl. Surf. Sci.* 498 (2019) 143876, <https://doi.org/10.1016/j.apsusc.2019.143876>.
- [10] L.A. Miya, L.F. Koao, S.V. Motloung, D.D. Hile, H.C. Swart, T.E. Motaung, Structure and optical properties of Er³⁺ doped ZnSe nanoparticles, *Opt. Mater.* 157 (2024) 116339, <https://doi.org/10.1016/j.optmat.2024.116339>.
- [11] T. Gupta, R.P. Chauhan, Optical, dielectric and photocatalytic properties of ZnO, ZnSe, and ZnO/ZnSe photocatalyst, *Opt. Mater.* 142 (2023) 114045.
- [12] H.K. Sadekar, A.V. Ghule, R. Sharma, Nanocrystalline ZnSe thin films prepared by solution growth technique for photosensor application, *Compos. B Eng.* 44 (2013) 553–557, <https://doi.org/10.1016/j.compositesb.2012.03.003>.
- [13] J. Ke, R. Zhang, P. Zhang, R. Yu, X. Cao, P. Kuang, B. Wang, Investigation on structural and optical properties of ZnSe thin films prepared by selenization, *Superlattice. Microst.* 156 (2021) 106965, <https://doi.org/10.1016/j.spmi.2021.106965>.
- [14] Sh Ozaki, K. Matsumoto, Growth of ZnSe nanowires on quartz substrates and their photomodulated transmittance spectra, *J. Phys. Chem. Solid.* 127 (2019) 115–118, <https://doi.org/10.1016/j.jpcs.2018.11.026>.
- [15] Li Yi, Chong Zhang, Jie Tian, Liang Wu, Guo-Qiang Liu, Hui-Hui Li, Yu-Zhuo Zhang, Zhen-Chao Shao, Zhen He, Shu-Hong Yu, On-demand synthesis of high-quality, blue-light-active ZnSe colloidal quantum wires, *Natl. Sci. Rev.* 9 (2022) nwac025, <https://doi.org/10.1093/nsr/nwac025>.
- [16] S. Jayalakshmi, M. Mariappan, M. Djanaguiraman, A. Veerappan, Aqueous soluble zinc selenide quantum dots for rapid detection of lead in water, fruit juices and biological fluids, *Opt. Mater.* 149 (2024) 115080, <https://doi.org/10.1016/j.optmat.2024.115080>.
- [17] D. Shi, Z. Guo, N. Bedford, Semiconductor quantum dots, in: Donglu Shi, Zizheng Guo, Nicholas Bedford (Eds.), *Micro and Nano Technologies, Nanomaterials and Devices*, William Andrew Publishing, 2015, pp. 83–104, <https://doi.org/10.1016/B978-1-4557-7754-9.00004-4>.
- [18] R. Cingolani, M. Lomascolo, N. Lovergine, M. Dabbico, M. Ferrara, I. Suemune, Excitonic properties of ZnSe/ZnS superlattices, *Appl. Phys. Lett.* 64 (1994) 2439–2441, <https://doi.org/10.1063/1.111592>.
- [19] D. Fisher (Ed.), *Defects and Diffusion in II-VI Compounds*, Trans Tech Publications Ltd, 1999.
- [20] J.H. Harding, A.M. Stoneham, Defect energies in ZnSe, *J. Phys. C Solid State Phys.* 15 (1982) 4649–4659, <https://doi.org/10.1088/0022-3719/15/22/011>.
- [21] Y. Wu, K.J. Mirrieles, D.L. Irving, On native point defects in ZnSe, *Appl. Phys. Lett.* 120 (2022), <https://doi.org/10.1063/5.0092736>.
- [22] W. Zheng, K. Singh, Z. Wang, J.T. Wright, J. Van Tol, N.S. Dalal, R.W. Meulenberg, G.F. Strouse, Evidence of a ZnCr₂Se₄ spinel inclusion at the core of a Cr-doped ZnSe quantum dot, *J. Am. Chem. Soc.* 134 (2012) 5577–5585, <https://doi.org/10.1021/ja210285p>.
- [23] K. Lamonova, I. Ivanchenko, S. Orel, S. Paranchich, V. Tkach, E. Zhiltukhina, N. Popenko, Yu. Pashkevich, Spectroscopic evidence of spinel phase clustering in solid solutions Hg_{1-x}Cr_xSe (0.03 ≤ x ≤ 0.1), *J. Phys. Condens. Matter* 21 (2009) 045603, <https://doi.org/10.1088/0953-8984/21/4/045603>.
- [24] S. Sheokand, D.S. Ahlawat, A. Singh, Nickel doped zinc selenide nanoparticles for spin based dilute magnetic semiconductor applications, *Micro and Nanostructures* 185 (2024) 207711, <https://doi.org/10.1016/j.micrma.2023.207711>.
- [25] K.V. Lamonova, S. Orel, A. Prokhorov, N. Kovalenko, M. Schmidbauer, A. Kwasniewski, Yu. Kazarinov, J.W. Tomm, ZnSe:(Cr,Fe) laser crystal matrices: challenges related to doping, *Opt. Mater. X* 22 (2024) 10032, <https://doi.org/10.1016/j.omx.2024.100321>.
- [26] K.V. Lamonova, S.M. Orel, Yu.G. Pashkevich, *Modified crystal field theory and its applications*, PH “Akademperiodyka, Kyiv, Ukraine, 2019, 10.15407/akademperiodyka.377.224.
- [27] A. Erba, J.K. Desmarais, S. Casassa, B. Civalieri, L. Donà, L.J. Bush, B. Searle, L. Maschio, L.-E. Daga, A. Cossard, C. Ribaldone, E. Ascrizzi, N.L. Marana, J.-P. Flament, B. Kirtman, CRYSTAL23: a program for computational solid state physics and chemistry, *J. Chem. Theor. Comput.* 19 (2023) 6891–6932, <https://doi.org/10.1021/acs.jctc.2c00958>.
- [28] M. Schmidbauer, A. Kwasniewski, J. Schwarzkopf, High-precision absolute lattice parameter determination of SrTiO₃, DyScO₃ and NdGaO₃ single crystals, *Acta Crystallogr. Sect. B Struct. Sci.* 68 (2012) 8–14, <https://doi.org/10.1107/S0108768111046738>.
- [29] S. Stoll, A. Schweiger, EasySpin, a comprehensive software package for spectral simulation and analysis in EPR, *J. Magn. Reson.* 178 (2006) 42–55, <https://doi.org/10.1016/j.jmr.2005.08.013>.
- [30] S. Stoll, Computational modeling and least-squares fitting of EPR spectra, in: S. K. Misra (Ed.), *Multifrequency Electron Paramagnetic Resonance*, 2014, <https://doi.org/10.1002/9783527672431.ch3>.
- [31] G.E. Hite, D.T.F. Marple, M. Aven, B. Segall, Excitons and the absorption edge in ZnSe, *Phys. Rev.* 156 (1967) 850–859, <https://doi.org/10.1103/PhysRev.156.850>.
- [32] J. Gutowski, K. Sebald, T. Voss, in: U. Rössler (Ed.), *SpringerMaterials, ZnSe: Bound Excitons*, Landolt-Börnstein - Group III Condensed Matter, 44C (New Data and Updates for III-V, II-VI and I-VII Compounds), 2010, https://doi.org/10.1007/978-3-540-92140-0_337.
- [33] A. Pawlis, M. Panfilova, D.J. As, K. Lischka, K. Sanaka, T.D. Ladd, Y. Yamamoto, Lasing of donor-bound excitons in ZnSe microdisks, *Phys. Rev. B* 77 (2008) 53304, <https://link.aps.org/doi/10.1103/PhysRevB.77.153304>.
- [34] G. Xing, J. Luo, H. Li, B. Wu, X. Liu, C.H.A. Huan, H.J. Fan, T.C. Sum, Ultrafast exciton dynamics and two-photon pumped lasing from ZnSe nanowires, *Adv. Opt. Mater.* 1 (2013) 319–326, <https://doi.org/10.1002/adom.201200045>.
- [35] C. Wang, S. Zhou, S. Xu, Z. Wang, Y. Cui, Discriminative detection of bivalent Cu by dual-emission ZnSe quantum dot fluorescence sensing via ratiometric fluorescence measurements, *Nanotechnology* 25 (2014) 375602, <https://doi.org/10.1088/0957-4484/25/37/375602>.
- [36] T. Takagahara, K. Takeda, Theory of the quantum confinement effect on excitons in quantum dots of indirect-gap materials, *Phys. Rev. B* 46 (1992) 15578–15581, <https://doi.org/10.1103/PhysRevB.46.15578>.
- [37] J. Pejchal, V. Babin, M. Buryi, V. Laguta, F. Hájek, J. Páterek, L. Procházková-Prouzová, L. Havlík, V. Czerneková, V. Vaněček, V. Doležal, J. Havlíček, K. Ruběšová, P. Zemenová, A. Falvey, R. Král, V. Pankratov, K. Chernenko, Untangling the controversy on Ce³⁺ luminescence in LaAlO₃ crystals, *Mater. Adv.* 3 (2022) 3500–3512, <https://doi.org/10.1039/D1MA01083B>.
- [38] V. Laguta, M. Buryi, J. Pejchal, K. Uličná, V. Římal, V. Chlan, H. Štěpánková, Y. Zagorodniy, M. Nikl, Incorporation of the Ce³⁺ activator ions in LaAlO₃ crystals: EPR and NMR study, *J. Solid State Chem.* 313 (2022) 123295, <https://doi.org/10.1016/j.jssc.2022.123295>.
- [39] J. Pejchal, V. Babin, M. Buryi, V. Laguta, F. Hájek, J. Páterek, L. Procházková-Prouzová, L. Havlík, V. Czerneková, V. Vaněček, V. Doležal, J. Havlíček, K. Ruběšová, P. Zemenová, A. Falvey, R. Král, V. Pankratov, K. Chernenko, Untangling the controversy on Ce³⁺ luminescence in LaAlO₃ crystals, *Mater. Adv.* 3 (2022) 3500–3512, <https://doi.org/10.1039/D1MA01083B>.
- [40] W. Nan, D. Yang, B. Zhou, L. Zhang, J. Xiao, H. Yu, Z. Hu, Y. Wu, Luminescence properties of Fe²⁺:ZnSe single crystals grown via a traveling heater method, *Crystals* 13 (2023) 411, <https://doi.org/10.3390/cryst13030411>.
- [41] K. Lamonova, B. Bekirov, I. Ivanchenko, N. Popenko, E. Zhiltukhina, V. Burkhovetskii, S. Orel, Yu. Pashkevich, Specific features of the temperature behavior of ESR spectra of Fe-doped mercury selenide, *Low Temp. Phys.* 40 (2014) 842–850, <https://doi.org/10.1063/1.4890988>.
- [42] K. Lamonova, S. Orel, Yu. Pashkevich, B. Bekirov, M. Hidulianov, I. Ivanchenko, N. Popenko, N. Kovalenko, A. Prokhorov, Y. Hizhnyi, S. Nedilko, N. Klyui, Temperature-induced charge transfer in Fe-doped ZnSe single crystal: mechanism and features, *Eur. Phys. J. Plus.* 137 (2022) 1018, <https://doi.org/10.1140/epjp/s13360-022-03237-x>.
- [43] Z. Wilamowski, W. Jantsch, G. Hendorfer, Electron paramagnetic resonance and Coulomb gap in HgSe:Fe, *Semicond. Sci. Technol.* 5 (1990) S266–S269, <https://doi.org/10.1088/0268-1242/5/3S/058>.
- [44] Z. Wilamowski, A. Mycielski, W. Jantsch, G. Hendorfer, Spin dynamics in the mixed-valence compound HgSe:Fe, *Phys. Rev. B* 38 (1988) 3621(R), <https://doi.org/10.1103/PhysRevB.38.3621>.
- [45] I.M. Tsidil'kovskii, Zero-gap semiconductors with magnetic impurities forming resonance donor states, *Sov. Phys. Usp.* 35 (1992) 85–105, <https://doi.org/10.1070/PU1992v035n02ABEH002215>.
- [46] M. Ernzerhof, G.E. Scuseria, Assessment of the Perdew–Burke–Ernzerhof exchange–correlation functional, *J. Chem. Phys.* 110 (1999) 5029–5036, <https://doi.org/10.1063/1.478401>.
- [47] C. Adamo, V. Barone, Toward reliable density functional methods without adjustable parameters: the PBE0 model, *J. Chem. Phys.* 110 (1999) 6158–6170, <https://doi.org/10.1063/1.478522>.
- [48] D.V. Oliveira, J. Laun, M.F. Peintinger, T. Bredow, BSSE-correction scheme for consistent Gaussian basis sets of double- and triple-zeta valence with polarization quality for solid-state calculations, *J. Comput. Chem.* 40 (2019) 2364–2376, <https://doi.org/10.1002/jcc.26013>.
- [49] H. Stoll, B. Metz, M. Dolg, Relativistic energy-consistent pseudopotentials—recent developments, *J. Comput. Chem.* 23 (2002) 767–778, <https://doi.org/10.1002/jcc.10037>.
- [50] J.K. Desmarais, J.P. Flament, A. Erba, Spin-orbit coupling in periodic systems with broken time-reversal symmetry: Formal and computational aspects, *Phys. Rev. B* 101 (2020) 235142, <https://doi.org/10.1103/PhysRevB.101.235142>.
- [51] J.K. Desmarais, J.P. Flament, A. Erba, Spin-orbit coupling from a two-component self-consistent approach. I. Generalized Hartree-Fock theory, *J. Chem. Phys.* 151 (2019) 074107, <https://doi.org/10.1063/1.5114901>.
- [52] J.K. Desmarais, J.P. Flament, A. Erba, Fundamental role of fock exchange in relativistic density functional theory, *J. Phys. Chem. Lett.* 10 (2019) 3580–3585, <https://doi.org/10.1021/acs.jpclett.9b01401>.
- [53] J.K. Desmarais, J.P. Flament, A. Erba, Adiabatic connection in spin-current density functional theory, *Phys. Rev. B* 102 (2020) 235118, <https://doi.org/10.1103/PhysRevB.102.235118>.
- [54] J.K. Desmarais, S. Komorovsky, J.P. Flament, A. Erba, Spin-orbit coupling from a two-component self-consistent approach. II. Non-collinear density functional theories, *J. Chem. Phys.* 154 (2021) 204110, <https://doi.org/10.1063/1.5114902>.
- [55] N. Chestnoy, R. Hull, L.E. Brus, Higher excited electronic states in clusters of ZnSe, CdSe, and ZnS: spin-orbit, vibronic, and relaxation phenomena, *J. Chem. Phys.* 85 (1986) 2237–2242, <https://doi.org/10.1063/1.451119>.
- [56] J.R. Shallenberger, N. Hellgren, Zinc selenide analyzed by XPS, *Surf. Sci. Spectra* 27 (2020) 014020, <https://doi.org/10.1116/6.0000165>.

- [57] S.B. Zhang, J.E. Northrup, Chemical potential dependence of defect formation energies in GaAs: application to Ga self-diffusion, *Phys. Rev. Lett.* 67 (1991) 2339, <https://doi.org/10.1103/PhysRevLett.67.2339>.
- [58] M. Chen, Ch Hu, W. Li, Huamin Kou, J. Li, Yu Pan, B. Jiang, Cr³⁺ in diffusion doped Cr²⁺:ZnS, *Ceram. Int.* 40 (2014) 7573–7577, <https://doi.org/10.1016/j.ceramint.2013.11.092>.
- [59] K. Lamonova, I. Danilenko, G. Volkova, S. Orel, Yu. Pashkevich, A. Prokhorov, O. Viagin, P. Maksimchuk, V. Seminko, Y. Malyukin, V. Kurnosov, Luminescence mechanism of Sm doped MgAl₂O₄ nanophosphors: role of nanoparticle size, samarium content and structural defects, *J. Lumin.* 241 (2022) 118493, <https://doi.org/10.1016/j.jlumin.2021.118493>.
- [60] I.I. Sobel'man, *Introduction to the Theory of Atomic Spectra*, Pergamon Press, New York, 1972, <https://doi.org/10.1016/C2013-0-02394-8>.
- [61] T.M. Dunn, *Trans. Faraday Soc.* 57 (1961) 1441–1444, <https://doi.org/10.1039/TF9615701441>.
- [62] E. Francisco, L. Pueyo, *Phys. Rev. A* 36 (1987) 1978–1982, <https://doi.org/10.1103/PhysRevA.36.1978>.
- [63] R.D. Shannon, Revised effective ionic radii and systematic studies of interatomic distances in halides and chalcogenides, *Acta Crystallogr., Sect. A* 32 (1976) 751–767, <https://doi.org/10.1107/S0567739476001551>.
- [64] A.A.B. Baloch, S.M. Alqahtani, F. Mumtaz, A.H. Muqabel, S.N. Rashkeev, F. H. Alharbi, Extending Shannon's ionic radii database using machine learning, *Phys. Rev. Mater.* 5 (2021) 1–10, <https://doi.org/10.1103/PhysRevMaterials.5.043804>.
- [65] L. Hou, C. Chen, L. Zhang, Q. Xu, X. Yang, M.I. Farooq, J. Han, R. Liu, Y. Zhang, L. Shi, B. Zou, Spin-related micro-photoluminescence in Fe³⁺ doped ZnSe nanoribbons, *Appl. Sci.* 7 (2017) 39, <https://doi.org/10.3390/app7010039>.
- [66] K. A. Jeong, S. Ku Lee, and NoSoung Myoung, Time-resolved spectroscopy of Fe³⁺ d-d transition in bulk ZnSe polycrystal, *Opt. Mater. Express* 9 (2019) 2964–2970, <https://doi.org/10.1364/OME.9.002964>.
- [67] R. Rai, J.Y. Savard, B. Tousignant, Evidence of inversion splitting in Cr³⁺ ion doped in ZnSe, *Phys. Lett. A* 25 (1967) 443, [https://doi.org/10.1016/0375-9601\(67\)90070-9](https://doi.org/10.1016/0375-9601(67)90070-9).
- [68] V.V. Fedorov, T. Konak, J. Dashdorj, M.E. Zvanut, S.B. Mirov, Optical and EPR spectroscopy of Zn:Cr:ZnSe and Zn:Fe:ZnSe crystals, *Opt. Mater.* 37 (2014) 262–266, <https://doi.org/10.1016/j.optmat.2014.06.004>.
- [69] J.F. Suyver, S.F. Wuijster, J.J. Kelly, A. Meijerink, Luminescence of nanocrystalline ZnSe:Mn²⁺, *Phys. Chem. Chem. Phys.* 2 (2000) 5445, <https://doi.org/10.1039/B006950G>.
- [70] H. Waldmann, C. Benecke, W. Busse, H.-E. Gumlich, A. Krost, The luminescence of the semimagnetic semiconductor Zn_{1-x}Mn_xSe, *Semicond. Sci. Technol.* 4 (1989) 71, <https://doi.org/10.1088/0268-1242/4/2/003>.
- [71] B. Yang, The photoluminescent and magnetic properties of Mn²⁺ ions at the interface of core/shell Mn-doped nanocrystals, *Int. J. Nanoparticles Nanotech.* 3 (2017) 9, <https://doi.org/10.35840/2631-5084/5509>.
- [72] Ck Muntaz Begum, G. Nirmala, K. Ravindranadh, T. Aswani, M.C. Rao, P. Sambasiva Rao, R.V.S.S.N. Ravikumar, Physical and spectral investigations of Mn²⁺ ions doped poly vinyl alcohol capped ZnSe nanoparticles, *J. Mol. Struct.* 1006 (2011) 344–347, <https://doi.org/10.1016/j.molstruc.2011.09.030>.